

Supporting Information for

Optimizing 1- μ s-Resolution Single-Molecule Force Spectroscopy on a Commercial Atomic Force Microscope

Devin T. Edwards, Jaevyn K. Faulk, Aric W. Sanders, Matthew S. Bull,
Robert Walder, Marc-Andre LeBlanc, Marcelo C. Sousa,
and Thomas T. Perkins

Contents:

Methods: Focused-ion-beam modification of cantilevers; Custom-detection module featuring a 3- μ m circular-spot size; Laser current modulation to reduce optical interference; Cantilever calibration; Characterizing ultrashort cantilever performance in liquid; Sample preparation; and Data acquisition and analysis.

Supporting Table 1: Mechanical properties of cantilevers during SMFS experiments.

Supporting Table 2: Beam parameters for FIB-modification of cantilevers.

Supporting Figure 1: Modifying ultrashort cantilevers with an FIB.

Supporting Figure 2: Reduced interference artifact using custom-detection module.

Supporting Figure 3: Stability and noise floor of detection modules.

Supporting Figure 4: Custom-detection module improves sensitivity of an ultrashort cantilever.

Supporting Movie 1: FIB-modification process.

Focused-ion-beam modification of ultrashort cantilevers

The overall FIB-modification process was conceptually similar to earlier work from our lab on longer cantilevers.¹ Critically, in this work, we optimized the process to reduce the bending of ultrashort cantilevers [BioLever Fast (AC10DS, Olympus)] so the modified ultrashort cantilevers could be detected. We modified ultrashort cantilevers on two different FIB instruments: an FEI Nova Nanolab 600, and the Zeiss Auriga. In general, the overall modification process was similar for both instruments, but the details were slightly different. We first describe the protocol for the FEI FIB and then discuss the differences in the protocol for the Zeiss. For ease of adoption, we also provide key parameters for both machines in Supporting Information Table S2.

Initially, we imaged the cantilever with the scanning electron microscope (SEM) on the FEI to align the cantilever (Figure S1a). The next step was to briefly image the cantilever with the FIB. This imaging allowed us to define the path for the Ga⁺ beam to cut a rectangular area ($\sim 4 \times 1.3 \mu\text{m}^2$) out of the ultrashort cantilever. Specifically, we used a series of three sequential cuts to remove the rectangular section. The beam parameters were 30 kV, 9.7 pA, and 1 $\mu\text{s}/\text{point}$ with a 50% beam overlap between successive points. The completion of each cut was monitored in real time via concurrent SEM imaging. The first modification consisted of two 4- μm -long cuts parallel to the cantilever's long axis (Figure S1b). The line segments were extended slightly (200 nm) into the edge of the chip supporting the cantilever to ensure the cantilever was cut all the way to its base support. Next, a single cut connected the first two cuts approximately halfway up the cantilever (Figure S1c). The third and final cut occurred at the base of the cantilever and generally caused the rectangular section to fold up and out of the way (Figure S1d). Moreover, such a folded flap often detached from the cantilever when immersed in liquid. Even in the absence of such detachment, a folded flap did not interfere with optical detection of the cantilevers.

Overall, this process yielded a modified cantilever with two narrow supporting beams that were 250–500-nm wide and 4- μm long. For a rectangular cantilever, the cantilever stiffness k decreases linearly with the cantilever width (w). This scaling relation suggests that our modification should have reduced k by a factor of 3. Instead, we measured a reduction in k closer to 2, most likely because the effective length of the cantilever was also reduced. As mentioned in the main text, this FIB-modification of the cantilevers also led to an unwanted upward bending of the cantilevers (Figure S1d). Cantilevers with more than a 5° bend prevented the reflected laser beam from being centered on the AFM's quadrant photodiode (QPD).

Several steps were taken to reduce this bending in the initial modification process. The first step was to minimize the number of times the cantilever was imaged with the ion beam (preferably to one). However, even a single imaging of the ultrashort cantilevers with the ion beam led to measurable bending. We therefore localized the imaging-induced bending to the section of the cantilever to be modified (*i.e.*, the 4 μm closest to the cantilever's base). Importantly, such localized imaging essentially left unbent the free end of the cantilever used to reflect the detection laser.

Despite the aforementioned efforts to reduce bending, most of these FIB-modified cantilevers were too bent to be detected. Fortuitously, we observed that thinning the remaining narrow supports with a defocused ion beam bent the cantilever in the opposite direction. On the FEI, such thinning of both cantilever supports was done concurrently (with parallel milling) using line segments that extend slightly ($\sim 0.2 \mu\text{m}$) into the chip with the same beam parameters used above, except the beam was manually defocused by $\sim 0.5 \text{ mm}$. To achieve a straight cantilever, we imaged the cantilever with the SEM during thinning. In general, an approximately straight cantilever was achieved after $< 5 \text{ s}$ of thinning (Figure S1e). Further thinning had varying results. Often, the

cantilever remained approximately straight for a cumulative total thinning time of 15–25 s. Typically, when the thinning time exceeds 25 s, the cantilever began to bend significantly, though the direction and temporal onset of bending was variable. Hence, we closely monitored the process and stopped the thinning at the onset of undesirable bending, even if the nominal amount of thinning for a desired k was not achieved (see below). Overall, this process dramatically increased the yield of straight and, therefore, detectable cantilevers.

Thinning had the added benefit of further reducing cantilever stiffness (k) since $k \propto T^3$, where T is the cantilever thickness. The final stiffness was roughly controlled by varying the total thinning time. However, achieving a precise stiffness for an individual cantilever was impractical because of the variable response of each cantilever to FIB modification. The overall FIB-modification process led to a 3–8-fold reduction in k , with a typical target stiffness of 20–40 pN/nm.

FIB-modification using the Zeiss instrument followed a conceptually similar process but with a slight change in the order of making the cuts. The first cut occurred approximately halfway up the cantilever and parallel to the short axis of the cantilever. Next, two longer slits were cut sequentially. As on the FEI, the final cut occurred at the base of the cantilever and induced upward bending of a rectangular flap. Beam parameters were 30 kV beam voltage, 2 pA, and 1 ms/point with a 50% beam overlap between points. The Zeiss Nanopatterning and Visualization Engine (NPVE) was used for all modifications. This feature allowed the line intensity to be monitored as a function of ion dosage during milling with the line intensity increasing with dosage until breakthrough was deduced by a drop in scattered secondary electrons. Using this process, we determined the ion dosage needed to fully mill through the cantilever. We note that the required dosage varied significantly between different cantilevers of the same type, but was typically between (0.06–0.10 nC/ μm^2).

The thinning process on the Zeiss FIB also had minor changes. First, the ion beam was raster scanned over two rectangular areas oriented along the thin cantilever supports. Beam parameters were 2 pA, 1 μ s/point dwell time, and 50% beam overlap. At these conditions, the thinning occurred more slowly than on the FEI FIB. The initial relaxation towards a straight cantilever typically occurred over \sim 45 s, while thinning longer than \sim 300 s often resulted in cantilevers that were too bent to be detected on our AFM. Hence, as on the FEI, we imaged each cantilever with the SEM during cutting and thinning to improve yield.

Custom-detection module featuring a 3- μ m circular-spot size

In general, the detection and use of a standard ultrashort cantilever (*e.g.*, BioLever Fast) require an AFM with a cantilever-detection-laser system that generates a spot size approximately the size of the cantilever.^{2,3} A useful feature of our commercial AFM (Cypher, Asylum Research) is that its small spot-size module (SLD-SS, Asylum Research) generated a laser focus ($9 \times 3 \mu\text{m}^2$) that approximately matched the dimensions of an unmodified BioLever Fast ($9 \times 2 \mu\text{m}^2$) and thereby facilitated its detection. However, the reduced size of our FIB-modified ultrashort cantilever led to reduced sensitivity (mV/nm) in comparison to an unmodified cantilever when using this commercial detection module (*e.g.*, 11 mV/nm vs 1.5 mV/nm, respectively)(Figure 2e and Figure S4). Analysis of the resulting records of thermal motion in liquid yielded uninterpretable power spectral densities (PSDs) that prevented standard calibrations of k (Figure 2d, *red*).

Hence, to detect these modified cantilevers on our commercial AFM, we developed a home-built cantilever-detection module that featured a 3- μ m diameter circular spot size well matched to the remaining size of our modified cantilever (Figure 2a). To achieve this spot size using our commercial AFM's existing optics, we needed a circular laser beam with a 4-mm diameter in a TEM₀₀ mode. We achieved these specifications while also minimizing the modifications inside the

commercial AFM using a triplet collimator to introduce a laser via a single-mode polarization-maintaining fiber. To further minimize a variety of noise sources (*e.g.*, intensity, pointing, mode, and polarization noise), we adopted a modified version of the laser stabilization techniques that we previously developed for optical trapping⁴ and optically stabilized AFM⁵ applications.

A schematic of the optical system is shown in Figure 2a. Here, we detail the individual components. The detection laser was a fiber-coupled, 853-nm laser diode (QFLD-850-100S-PM, Q-Photonics). The laser was run at an average output power of ~ 20 mW. The drive current was modulated at ~ 465 MHz to reduce the effect of an optical-interference artifact common in detecting ultrashort cantilevers.⁶ The details of current modulation are specified in the next section. The output of the laser was launched into free space using a standard fiber launch (Fiberport PAF-X-5-B, Thorlabs) and passed through an optical isolator (IOQB-4D-850-VLP, Thorlabs). To coarsely set the intensity of the laser and achieve a pure polarization of the beam, we next passed the laser through a $\lambda/2$ -wave plate (RABH-980, Thorlabs) and polarizing beam splitter [PBS (05FC16PB.5, Newport)]. We intensity stabilized the laser using an acousto-optic modulator [AOM (1205C, Isomet)] mounted on a 6-axis tilt-tip mount (9071, Newport). A second PBS repolarized the beam before coupling into a single-mode polarization-maintaining fiber that contained a 50/50 split fiber (954P, Evanescent Optics). One output arm was used to stabilize the laser intensity after fiber coupling, and the other arm was used to launch the laser inside of the commercial AFM. In order to achieve spatial mode filtering by the single-mode fiber, we used a 6 m long fiber with the fiber split positioned at the center of the fiber's length.

The intensity stabilization used an analog-feedback loop that varied the intensity of the sound wave in the AOM in response to changes in laser intensity measured using a photodiode [PD (YAG-444AH, Excelitas Technologies)] located at one fiber output arm. As discussed in prior

work,⁴ this set of optics converts a variety of noise sources (including pointing noise, polarization fluctuations, and mode noise) into intensity noise. Though conceptually identical to our prior stabilization scheme,⁴ the present use of a fiber splitter minimized the optics within the commercial AFM by sampling the beam at a location spatially removed from the final laser output.

Pointing noise of the cantilever detection laser degrades optical-lever-arm performance. So, we minimized the pointing noise by mechanically supporting the fiber at two locations inside the AFM. In essence, this mounting isolated the end of the fiber from small, inadvertent motion of the thin flexible fiber. The first support was formed by a slit in a piece of foam between the inside and the outside of the AFM housing. The second support was a Delrin tube also containing a slit piece of foam that supported the fiber 10 cm before fiber launch (*i.e.*, the end of the fiber).

We launched the laser into free space inside the AFM using a triplet collimator with a focal length of 18 mm and aligned for 850 nm (TC-18APC, ThorLabs). We supported the collimator using a simple custom-machined metal mount that mated our collimator into the existing mounting interface used for the different detection modules supported by our commercial AFM. The focal length of the collimator was chosen to produce a Gaussian, circular beam of ~4 mm in diameter. The rest of the AFM optics remained unchanged. Overall, this mounting scheme allowed us to exchange our custom small-spot detection module with either of our two commercial detection modules (small and standard spot size) in ~20 min.

Our active intensity stabilization significantly improved the stability of the detection laser intensity as measured by the AFM's QPD as compared to the unstabilized laser (Figure S3a). To demonstrate this improvement, we reflected the detection laser off the chip supporting the ultrashort cantilever and digitized the sum signal (*i.e.*, the total laser intensity on the QPD) at 50 kHz for 100 s. We quantified the resulting signal using the standard deviation of the normalized

sum signal. Our active stabilization decreased intensity fluctuation 33-fold to 4.5×10^{-5} , as deduced by this metric.

Analysis of the cantilever deflection signal's noise floor shows that our home-built detection module has a 20-fold better detection sensitivity at higher frequency (>10 kHz) compared to the commercial small spot-size module. To do this analysis, we rezeroed the deflection signal using the automated routine in the commercial AFM. After which, we digitized the deflection signal at 5 MHz for 20 s when reflecting the laser of the cantilever chip. We scaled the resulting deflection signal by the sensitivity of a typical FIB-modified cantilever to yield our estimate of the instrumental noise floor (Figure 2e, *black*). We next computed the raw *voltage* power spectral densities (PSDs) from 22 sequential sections of a 20-s trace and deduced an averaged PSD from these individual PSDs. As shown in Figure S3b, the voltage PSDs of the deflection signal show that our custom-detection module equals the performance of the commercial small spot-size module at low frequencies. At higher frequencies (>10 kHz), our noise floor was 20-fold lower than the commercial small spot-size unit. We emphasize that this estimate of the noise floor does not account for additional 3–5 fold higher sensitivity for detecting modified ultrashort cantilevers with the two different detection lasers (Figure 2e). For sufficiently large cantilevers, the commercial module provided better detection sensitivity, as expected.³ Finally, we note that the custom-built detection module led to improved performance of the optical-lever-arm system for both FIB-modified (Figure 2e) and standard ultrashort cantilevers (Figure S4).

We note that our custom-detection module had a similar low-frequency deflection noise floor in the absence of intensity stabilization (Figure S3b, *purple*), suggesting intensity noise was not the primary source of the low-frequency instrumental noise seen to dominate the behavior of optical-lever-arm detection.⁷

Laser current modulation to reduce optical interference

To reduce the optical-interference artifact that obscures the deflection signal, we modulated the laser-diode current at high frequencies ($\sim 465\text{--}500$ MHz), which broadens the laser's spectral linewidth.⁸ This broadening reduced the interference artifact by decreasing the effective coherence length of a laser diode. Specifically, we utilized a tunable 280–625 MHz oscillator (ZX95-625-S+, Mini-Circuits) at ~ 465 MHz. The oscillating signal was passed through a voltage-controlled, variable attenuator (ZX73-2500-S+, Mini-Circuits) and a fixed, ~ 18 dB amplifier (ZX60-P103LN+, Mini-Circuits). The oscillating signal was then AC-coupled into the laser diode current drive using a bias-tee (ZFBT-4R2G+, Mini-Circuits). A 4-port directional coupler (ZFBDC20-62HP-S+, Mini-Circuits) and 2 power meters (ZX47-40-S+, Mini-Circuits) allowed both the forward and reflected power to be monitored. In our hands, we found the best performance when the unit was run at full power (minimum attenuation) along with a DC current of 50 mA. At these drive parameters, we experienced no damage to the laser diode. Further reduction of the interference artifact is possible at a higher-modulation depth. However, too strong a current modulation could reverse bias the laser diode, causing damage. As a consequence, we have not yet explored this limit.

Using this modulation scheme, we significantly reduced the observed interference effect (Figure S2). While the extent of the decrease depends on the focus position, tip geometry, and sample surface, we typically observed a 50% decrease in the amplitude of the oscillation. Interestingly, we also observed improved laser intensity stability in the absence of active feedback when applying the high-frequency modulation. We speculate that such modulation minimized the laser mode-hopping, in part, by reducing sensitivity of the diode laser to back reflections.

Cantilever calibration

We determined the cantilever stiffness k (pN/nm) for each cantilever and the optical-lever-arm sensitivity (mV/nm) prior to each individual use of that cantilever. Stiffness is an intrinsic property of the cantilever. Sensitivity depends on a variety of instrumental factors including lateral location, size, and vertical position of the detection laser focus on the cantilever.

For ultrashort cantilevers (both unmodified and FIB-modified), we deduced k in air. Determining k in air was simpler than in liquid due the cantilever's higher Q caused by less damping. This approach follows the general calibration approach outlined in the pioneering SMFS using ultrashort cantilevers.⁶ To preserve the cleanliness of the tip, we used freshly cleaved mica as the surface and positioned the cantilever 50 μm over the surface. We next positioned the laser focus on the back of the cantilever at the location that produced the maximum sensitivity. This position was determined by applying a small AC vertical amplitude to the base of the cantilever and finding the largest measured voltage amplitude on the QPD's deflection signal.

For the unmodified BioLever Fast, we calibrated k using the standard approach for rectangular cantilevers in air.⁹ Specifically, the PSD of the cantilever's thermal motion around the first harmonic was fit to a simple-harmonic oscillator (SHO).¹⁰ This method yields the cantilever quality factor (Q) and resonance frequency (f_c). These parameters, in conjunction with the known planar size of the cantilever ($9 \times 2 \mu\text{m}^2$), were then used to calculate k . Calibrating the cantilever in this way allows the amplitude of the SHO model to be used to determine the sensitivity in liquid.¹¹ However, the sensitivity can also be determined using the standard approach of gently pushing the cantilever into a hard surface. The resulting deflection signal as a function of vertical motion of the cantilever's base (*e.g.*, ZPZT) was fit to a line. The measured slope of that line yields the

sensitivity. The sensitivity determined from contact with freshly cleaved mica typically was within $\pm 15\%$ of the sensitivity determined from the SHO model.⁹

Modified cantilevers are not rectangular and thus not well described by the Sader method for rectangular cantilevers,⁹ therefore determination of k required a measurement of sensitivity. To do so, we gently pushed the cantilever into the mica surface as described above. We used this sensitivity to compute the thermally induced positional motion of the cantilever recorded at $50\ \mu\text{m}$ over the surface and then fit the PSD to a SHO to determine k . We averaged the spring constant measured at two or more different locations. Finally, each time a large change in z position was made (*i.e.*, following motion to and from $50\ \mu\text{m}$ over the surface), the laser position on the back of the cantilever was adjusted to re-maximize the deflection amplitude using the AC-oscillation scheme discussed above.

For deducing the sensitivity of ultrashort cantilevers in liquid, we analyzed the thermal motion of the cantilever far from the surface using the value for k deduced in air. This calibration scheme addressed two problems when trying to calibrate sensitivity for ultrashort cantilevers: (*i*) the adverse effect of the large interference artifact when trying to measure the sensitivity via the hard-contact scheme and (*ii*) the assumption of hard contact when pressing into a protein-coated surface. In the latter case, we observed variations in the sensitivity when pressing the PEG-coated cantilevers into PEG-coated surfaces. Pushing harder could correct these discrepancies, but we found that determining the sensitivity via a thermal measurement and a predetermined k yielded more consistent results, similar to the original SMFS work with ultrashort cantilevers.⁶

Longer cantilevers were significantly easier to calibrate. As a result, the long BioLever and modified BioLever Mini were calibrated in liquid immediately preceding the cantilever

characterization using standard procedures,¹⁰ including deducing sensitivity by pushing into the surface.

Characterizing ultrashort cantilever performance in liquid

In a typical AFM-based SMFS assay, the cantilever is very close to its surface. We therefore sought to characterize cantilevers in this regime where there is increased hydrodynamic drag due to squeezed-film damping.¹² To do so, we recorded the thermal motion in the zero force position (z_0) of the cantilever at 50 nm over the surface after the cantilever had been in liquid for >1 h. This metric, which we have previously used,^{1,13} includes the Brownian motion of the cantilever, low-frequency instrumental noise in the optical-lever-arm detection, and cantilever drift. For the modified and unmodified BioLever Fasts, the deflection signals were digitized for 20 s at 5 MHz. As discussed above, we divided the 20-s traces into 22 sections, calculated the individual PSD for each section, and then computed an average PSD. For the modified BioLever Mini and long BioLever, we recorded 100-s traces at 50 kHz. For these longer traces, we divided the traces into 18 segments and then computed an average PSD. We compared the performance between different cantilevers with different dimensions and stiffnesses by computing the average force precision over a specified averaging time (T) using the Allan deviation: $\sigma_x(T) = \sqrt{\frac{1}{2} \langle (\bar{x}_{i+1} - \bar{x}_i)^2 \rangle_T}$, where \bar{x}_i is the mean value of the data over the i^{th} time interval.¹⁴ For completeness, we note that the all of the cantilevers except the modified BioLever Mini were protein-coated (*see below*).

Sample preparation

In this work, we stretched a polyprotein consisting of four repeats of NuG2, conceptually similar to our previous study of the performance of a FIB-modified BioLever Mini¹ where we unfolded a

polyprotein consisting of eight repeats of NuG2.¹⁵ To improve efficiency, we used a specific-attachment protocol developed in our lab that covalently anchored a biotinylated polyprotein to a PEG-coated surface and used streptavidin anchored to PEG-coated cantilevers (unpublished data).

Data acquisition and analysis

All experiments were performed on a state-of-the-art commercial AFM (Cypher, Asylum Research) featuring a temperature-controlled closed fluidic chamber (Cypher ES, Asylum Research). All measurements were performed at 25 °C in 50 mM sodium phosphate (pH 7.0), 150 mM NaCl. For SMFS experiments, we initiated attachment by pressing into the surface at ~500 pN for 1 s and then retracted the tip at 400 nm/s. The exact force used to initiate attachment varied between cantilevers depending on the magnitude of the interference artifact. Data was collected concurrently at 50 kHz and 5 MHz and anti-aliased at 25 kHz and 2.5 MHz, respectively.

The first step in data processing was to digitally subtract out the interference artifact from the cantilever deflection signal. To do so, we developed an empirical formula that fit the deflection voltage (V_D) versus the vertical position of the piezo-electric stage (z_{PZT}) as the cantilever approached the surface (*e.g.*, the approach curve) to the function: $V_D = A_1 + A_2 * z_{PZT} + (A_3 + A_4 z_{PZT}) * \sin(A_5 + A_6 z_{PZT})$, where A_1 - A_6 are fit parameters over a typical region from 3–200 nm over the surface. We then used the coefficients determined from this fit to remove the optical-interference artifact from the individual pulling curves (*e.g.*, the retraction curves) over the same range. When this digital subtraction was applied to records without protein attachment, the resulting residual force offsets in the retraction records were <7 pN. We note that our formula is purely empirical rather than being based on a physical model. Over a limited z -range, sufficiently good fits can be generated using other parameterizations such as a polynomial fit with a sufficiently high number of coefficients.

We analyzed the resulting force-extension curves (FECs) using an improved numerical approximation¹⁶ for an inextensible worm-like chain (WLC) model.¹⁷ FECs for a wide variety of biopolymers including DNA¹⁸ and proteins¹⁹ have been well described by a WLC model. The WLC model is parameterized by the persistence length (p) and contour length (L_0) of the polymer. In our fits, we used $p = 0.4$ nm, a common value for AFM-based SMFS.^{19,20} As each protein domain in the polyprotein unfolds, the contour length should increase by a fixed length (ΔL_0) proportional to the number of the released amino acids. Therefore, in our analysis, we used two free parameters, ΔL_0 and L_{Final} , the contour length of the fully unfolded protein. This model was globally fit to each FEC by dividing it into segments corresponding to each unfolding event. We found that the final segment deviated from WLC behavior at $F > 150$ pN and therefore limited the upper force range in the WLC fit to 150 pN. This analysis yielded ΔL_0 of 17.9 nm (unmodified Fast), 17.7 nm (stiff modified Fast), and 17.3 nm (soft modified Fast), values consistent with the previously reported value of 17.6 nm.^{1,15,21} Finally, we note that deviation in our data from an ideal WLC model at higher forces is small by AFM-based SMFS standards, but warrants further study in future work.

The force precision while stretching a fully unfolded protein shown in Figure 3e was determined from a 40- μ s long force-versus-time record around 65 pN using the 5 MHz data. Prior to the histogram analysis, we subtracted off a linear tilt to the data. This process eliminated the slight increase in force due to the polyprotein being stretched during the 40- μ s time window.

Cantilever	L (μm)	k (pN/nm)	f_c (kHz)	Q	τ (μs)
BioLever Fast	9	130	465 ± 4	0.88 ± 0.01	0.4
Stiff modified BioLever Fast	9	40	272 ± 4	0.58 ± 0.01	1.2
Soft modified BioLever Fast	9	20	210 ± 6	0.50 ± 0.01	1.8

Table S1. Mechanical properties of cantilevers while stretching an unfolded protein. The cantilever length (L) is the typical length provided by manufacturer. The spring constant (k) was measured in air as described. A power spectral density (PSD) was calculated from the complete final portion of the unfolding curve corresponding to the fully unfolded polyprotein (*i.e.*, after the unfolding of the 4th NuG2 domain to tip detachment). These PSDs were fit to the simple harmonic oscillator function to yield the resonance frequency (f_c) and Q . The measured relaxation time (τ) was determined by fitting the decay in the force-versus-time record to an exponential (Figure 3c).

Settings	FEI Anova	Zeiss Auriga
SEM		
Voltage	5 kV	5 kV
Current	98 or 400 pA	98 or 400 pA
FIB		
Voltage	30 kV	30 kV
Cutting current	9.7 pA	2 pA
Cutting dwell time	1 μs	1 ms
Cutting beam overlap	50%	50%
Thinning current	9.7 pA	2 pA
Thinning dwell time	1 μs	1 μs
Thinning beam overlap	50%	50%
Thinning time	5–30 s	30–150 s
Thinning defocus	0.5 mm	0 mm

Table S2. Beam parameters for FIB-modification of cantilevers using the FEI Anova and Zeiss Auriga.

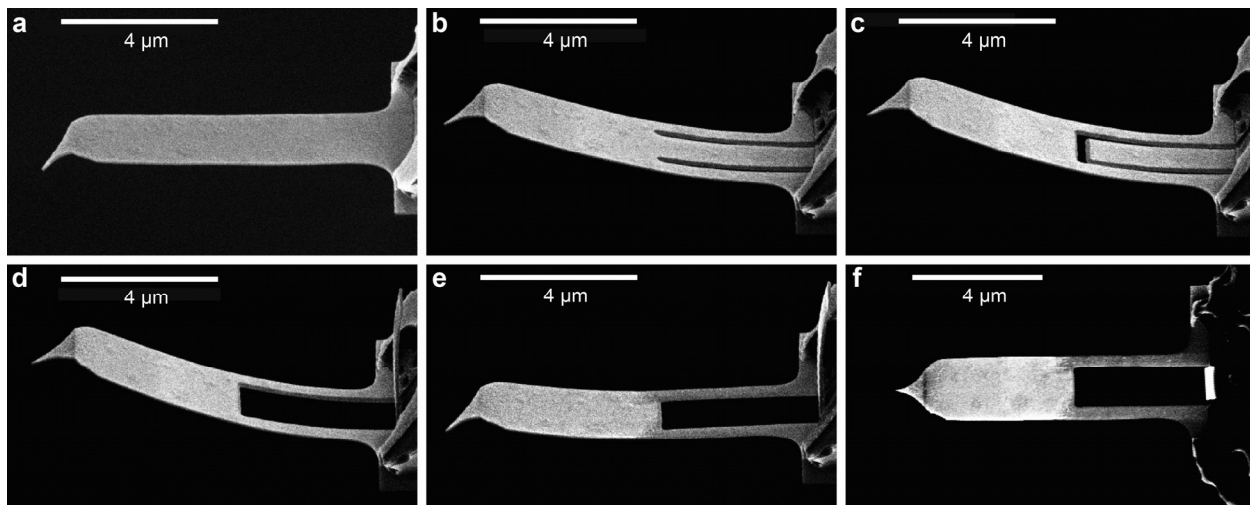


Figure S1. Modification of an ultrashort cantilever with a focused ion beam (FIB). Scanning electron microscope (SEM) images were taken during FIB-modification process. Images (a-e) are taken at 52° perspective. The cantilevers were normal to the ion beam during modification. (a) SEM image of an unmodified BioLever Fast. (b) Image after two lines were cut concurrently to define the rectangular area to be removed. (c) Image after another line was cut to release a rectangular flap from the rest of the cantilever. (d) Image after a cut along the base of the chip caused the flap to fold up. (e) Image after thinning the narrow cantilever supports using a defocused ion beam. The thinning relaxed the cantilever back towards normal. (f) Image of the fully modified cantilever at 0° .

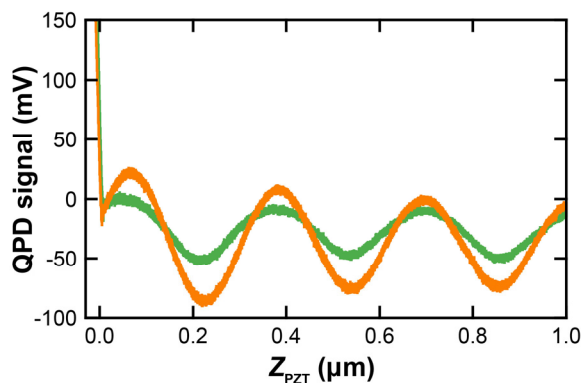


Figure S2. Current modulation reduces the effect of the interference artifact for modified ultrashort cantilevers. The QPD voltage is plotted as a function of Z_{PZT} within $1 \mu\text{m}$ of the surface with current modulation active (*green*) and disabled (*orange*).

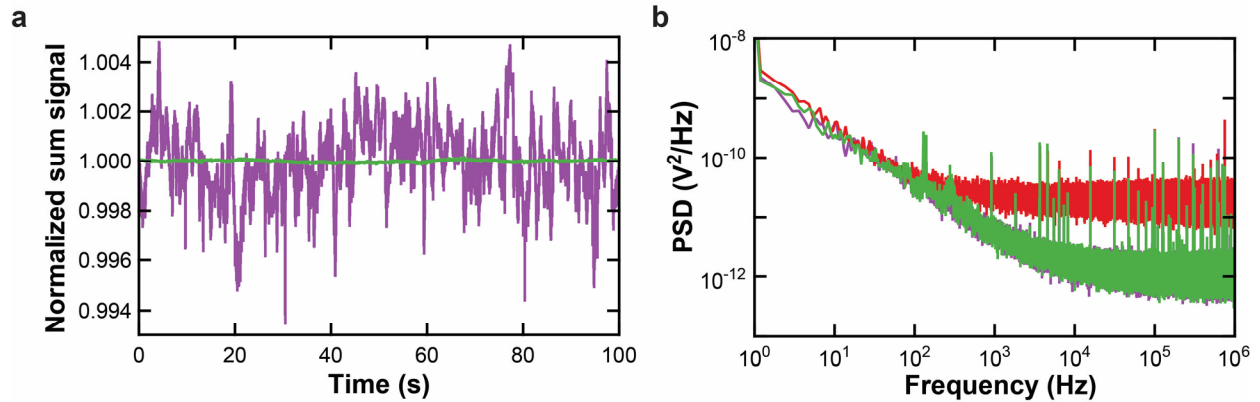


Figure S3. Stability and noise floor of detection modules. (a) The total laser light detected by the QPD as a function of time measured by reflecting the detection laser off a gold-coated AFM chip using our custom small spot-size laser module with (*green*) and without (*purple*) intensity stabilization. (b) The voltage power spectral density (PSD) of the deflection signal measured as a function of frequency recorded by bouncing the laser off the base a gold-coated AFM chip for the commercial small spot-size laser (*red*), and our custom small spot-size laser with (*green*) and without (*purple*) intensity stabilization. Note the purple trace is almost completely obscured by green trace. This overlap shows that deflection noise floor was essentially identical with and without intensity stabilization. To facilitate this comparison, each record was measured using the same sum signal on the QPD.

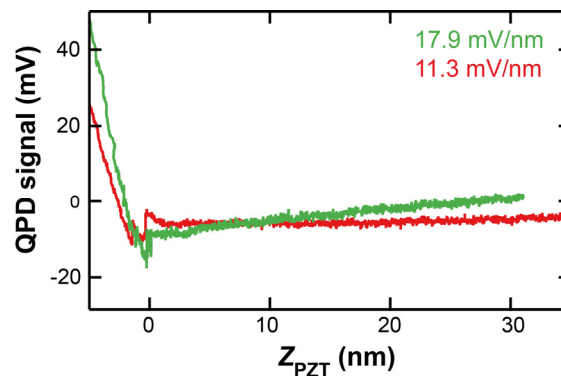


Figure S4. Custom-detection module provides 60% higher sensitivity than the commercial one with a standard ultrashort cantilever. The QPD voltage is plotted as a function of Z_{PZT} within 40 nm of the surface measured with our custom small spot-size laser (*green*) and the commercial small spot-size module (*red*). In this comparison, the laser intensity of the two different detector beams was set to the same value based upon the sum signal measured when reflecting the laser off the gold-coated chip. The resulting sum signal off of the cantilevers was the same to within 10%.

REFERENCES

- (1) Bull, M. S.; Sullan, R. M.; Li, H.; Perkins, T. T. *ACS Nano* **2014**, *8*, 4984-4995.
- (2) Viani, M. B.; Schaffer, T. E.; Chand, A.; Rief, M.; Gaub, H. E.; Hansma, P. K. *J. Appl. Phys.* **1999**, *86*, 2258-2262.
- (3) Fukuma, T.; Jarvis, S. P. *Rev. Sci. Instrum.* **2006**, *77*, 043701.
- (4) Carter, A. R.; King, G. M.; Ulrich, T. A.; Halsey, W.; Alchenberger, D.; Perkins, T. T. *Appl. Opt.* **2007**, *46*, 421-427.
- (5) King, G. M.; Carter, A. R.; Churnside, A. B.; Eberle, L. S.; Perkins, T. T. *Nano Lett.* **2009**, *9*, 1451-1456.
- (6) Rico, F.; Gonzalez, L.; Casuso, I.; Puig-Vidal, M.; Scheuring, S. *Science* **2013**, *342*, 741-743.
- (7) Sullan, R. M.; Churnside, A. B.; Nguyen, D. M.; Bull, M. S.; Perkins, T. T. *Methods* **2013**, *60*, 131-141.
- (8) Kassies, R.; van der Werf, K. O.; Bennink, M. L.; Otto, C. *Rev. Sci. Instrum.* **2004**, *75*, 689-693.
- (9) Sader, J. E.; Chon, J. W. M.; Mulvaney, P. *Rev. Sci. Instrum.* **1999**, *70*, 3967-3969.
- (10) Proksch, R.; Schaffer, T. E.; Cleveland, J. P.; Callahan, R. C.; Viani, M. B. *Nanotechnology* **2004**, *15*, 1344-1350.
- (11) Higgins, M. J.; Proksch, R.; Sader, J. E.; Polcik, M.; Mc Endoo, S.; Cleveland, J. P.; Jarvis, S. P. *Rev. Sci. Instrum.* **2006**, *77*, 013701.
- (12) Green, C. P.; Sader, J. E. *J. Appl. Phys.* **2005**, *98*, 114913.
- (13) Churnside, A. B.; Sullan, R. M.; Nguyen, D. M.; Case, S. O.; Bull, M. S.; King, G. M.; Perkins, T. T. *Nano Lett.* **2012**, *12*, 3557-3561.
- (14) Sullivan, D. B.; Allan, D. W.; Howe, D. A.; Walls, E. L., *Characterization of Clocks and Oscillators*. U.S. Government Printing Office: 1990.
- (15) Cao, Y.; Kuske, R.; Li, H. *Biophys. J.* **2008**, *95*, 782-788.
- (16) Bouchiat, C.; Wang, M. D.; Allemand, J.; Strick, T.; Block, S. M.; Croquette, V. *Biophys. J.* **1999**, *76*, 409-13.
- (17) Fixman, M.; Kovac, J. *J. Chem. Phys.* **1973**, *58*, 1564-8.
- (18) Bustamante, C.; Marko, J. F.; Siggia, E. D.; Smith, S. B. *Science* **1994**, *265*, 1599-1600.
- (19) Rief, M.; Gautel, M.; Oesterhelt, F.; Fernandez, J. M.; Gaub, H. E. *Science* **1997**, *276*, 1109-1112.
- (20) Carrion-Vazquez, M.; Oberhauser, A. F.; Fowler, S. B.; Marszalek, P. E.; Broedel, S. E.; Clarke, J.; Fernandez, J. M. *Proc. Natl. Acad. Sci. U.S.A.* **1999**, *96*, 3694-3699.
- (21) He, C.; Hu, C.; Hu, X.; Xiao, A.; Perkins, T. T.; Li, H. *Angew. Chem. Int. Edit.* **2015**, *54*, 9921-9925.